Deep into the core of dense star clusters: an astrometric and photometric test case for ELT

G. Fiorentino [1,2]★ M. Bellazzini [1] M. Spera [3,4,5] N. B. Sabha,[6] M. Mapelli [3,4,5,6]
L. Schreiber,[1] M. Dall'Ora,[7] L. Inno [8] M. Patti [1] V. F. Braga,[2] M. Lombini [1]
E. Diolaiti,[1] F. Cortecchia,[1] C. Arcidiacono,[3] C. Plantet[8] and G. Agapito[8]

[1]*INAF – Osservatorio di Astrofisica e Scienza dello Spazio di Bologna, via Gobetti 93/3, I-40129 Bologna, Italy*
[2]*INAF – Osservatorio Astronomico di Roma, via Frascati 33, I-00078 Monte Porzio Catone, Roma, Italy*
[3]*Dipartimento di Fisica e Astronomia G. Galilei, Università degli Studi di Padova, vicolo dell'Osservatorio 3, I-35122 Padova, Italy*
[4]*INFN – Padova, via Francesco Marzolo 8, I-35121 Padova, Italy*
[5]*INAF – Osservatorio Astronomico di Padova, vicolo dell'Osservatorio 5, I-35122 Padova, Italy*
[6]*Institute for Astro- and Particle Physics, University of Innsbruck, Technikerstr. 25, A-6020 Innsbruck, Austria*
[7]*INAF – Osservatorio Astronomico di Capodimonte, salita Moiariello 16, I-80131 Napoli, Italy*
[8]*INAF – Osservatorio Astronomico di Arcetri, Largo Enrico Fermi 5, I-50125 Firenze, Italy*

ABSTRACT

We present a novel analysis of a young star cluster in the Large Magellanic cloud, R136-like, as seen by the Extremely Large Telescope (ELT). The main aim of this study is to quantify precision and accuracy of stellar proper motion measurements in crowded field when using an ELT working at its diffraction limit. This can serve as a reference study for future development of ELT scientific cases. In particular, we investigate our future ability to detect the dynamical signature of intermediate-mass black holes (IMBHs) with mass $\sim 10^4\,\mathrm{M}_\odot$ through detailed measurements of stellar proper motions. We have simulated two *N*-body dynamical cluster models with and without an IMBH. For each model, we have chosen two snapshots temporally spaced by 5 yr. Stellar fluxes in *IJHK* filters and star positions have been used to create ELT mock images for both single- and multiconjugate adaptive optics observing modes following the requierements given by ESO technical specifications for the first light imager. These images have been analysed using a classical software for seeing-limited data reduction, DAOPHOT/ALLSTAR. We make accurate photometry till the very faint pre-main-sequence stars, i.e. depending on the adaptive optics (AO) mode, magnitudes down to $K \sim 24$ mag (single-conjugate AO) or $K \sim 22$ mag (multiconjugate AO) in a total integration time of 20 min on target. Although DAOPHOT suite of programs is not devoted to precise astrometry, the astrometric accuracy is impressive, reaching few μas yr^{-1} or km s^{-1}. In these assumptions, we are able to detect the IMBH signature at the centre of the cluster.

Key words: instrumentation: adaptive optics – galaxies: clusters – techniques: high angular resolution – techniques: photometric.

1 INTRODUCTION

In the near future, 30 m class telescopes will open a new window on the sky. The extreme spatial resolution offered by these giant telescopes will be unprecedented and will not be overcome for the next decades. Adaptive optics (AO) is the technology that will feed these giants to allow them to reach their diffraction limit from the ground, with the best performance expected for wavelengths

longer than one micron. The current possible spatial resolution, available with the *Hubble Space Telescope* (*HST*), is limited by the telescope diameter (*HST* diffraction limit is DL $\sim$ 0.06 arcsec in *I* band), and also, by the relatively large pixel size of the camera ($\sim$0.05 arcsec for both WFC3 and ACS). Nevertheless, the resulting astrometric accuracy is $\sim$500 μas (Anderson & King 2006). This is comparable with what is obtained by 10-m telescopes in infrared bands (Dalessandro et al. 2016; Massari et al. 2016b). In *K* band, a 39-m telescope offers a DL point spread function (PSF) of $\sim$0.012 arcsec FWHM. When equipped with a high-resolution imager like MICADO (Multi-AO Imaging Camera for Deep Observations;

Davies et al. 2016) with two possible pixel scales, 0.0015 and 0.004 arcsec per pixel, the astrometric accuracy is predicted to be better than 50 μas, thus comparable with *Gaia* in uncrowded stellar region. This means that the next generation of Extremely Large Telescopes (ELTs) is supposed to revolutionize our view of very dense and obscured stellar regions. Given the peculiar PSF shape provided by the AO technique and its variation across the field of view (FoV), a simple exposure time calculator is not enough to make detailed predictions on scientific cases; for this reason the best approach is to simulate ELT data.

In this study, we investigate the impact of ELT on the detection of intermediate-mass black holes (IMBHs) at the centre of star clusters. IMBHs are the missing link between stellar and supermassive black holes. They are supposed to be the most likely formation seeds of supermassive black holes hosted in giant galaxies and potentially driving galaxy assembly (e.g. Volonteri, Haardt & Madau 2003; Volonteri, Lodato & Natarajan 2008; Devecchi & Volonteri 2009; Boekholt et al. 2018, see Volonteri 2010 for a review). IMBHs might form in star clusters through several dynamical processes, such as runaway collisions among massive stars (Portegies Zwart & McMillan 2002; Portegies Zwart et al. 2004; Mapelli 2016; Di Carlo et al. 2019) and repeated mergers between stellar mass black holes (Miller & Hamilton 2002; Giersz et al. 2015). However, the observational confirmation of the existence of IMBHs in star clusters is still missing.

In this paper, we use *N*-body simulations of a star cluster to produce mock images of an ELT-like imager, hereafter ELTcam. In order to simulate the diffraction limit ELTcam images, we have used prescriptions from MAORY (the first light Multimode AO RelaY assisting ELT, Diolaiti 2016) and MICADO (Davies et al. 2016) in their current Phase B design.

In particular, we focus our attention on the young star cluster R136 in the Large Magellanic Cloud (LMC) which is ∼50 kpc away from us. Dense young clusters have been proposed as crucial scientific targets for ELTs (see e.g. Fiorentino et al. 2017, and references therein) since a high-resolution study of their core allows us to constrain their kinematics with unprecedented sensitivity on extremely small scales. R136 is located within one of the most spectacular star-forming regions of the local Universe, the 30 Doradus region (Tarantula nebula). Several studies, including an *HST* treasury project (Hubble Tarantula Treasury Projects, HTTP Sabbi et al. 2016), have been devoted to the detailed study of this region. However, even the deepest infrared observations, performed using WFC3 onboard of *HST*, were not able to explore the faintest ($F110W \geq 22$ mag) stars of the dense young cluster R136. Thus, R136 is the ideal candidate to be explored with the photometric and astrometric capabilities offered by an ELTcam. Transverse velocities are expected to be measured (from proper motions) with ∼2–5 km s^{-1} accuracy, enabling us to investigate the presence of an IMBH within the central parsec of the cluster.

Star clusters are also ideal targets for AO observations since there are plenty of bright stars that can naturally serve to guide the AO real time correction (natural guide stars, NGS). We have studied the sky coverage[1] on the 30 Doradus region using public HTTP catalogues (Sabbi et al. 2016). This near-infrared survey reaches $H \simeq 22.0$, thus fainter than the sensitivity limit of the current design of

MAORY wavefront sensors.[2] In the bright regime ($K \lesssim 13.0$) we complemented the HTTP catalogue with stars from 2MASS in the same area. With this final catalogue of candidate NGSs, by means of detailed simulations of the optical performances of ELTcam, we find that the sky coverage in this small spot of sky (∼2 arcmin × 2 arcmin) is virtually 100 per cent, and the typical Strehl ratio (SR)[3] is about 40 per cent, thus ensuring very good AO performance in the case under study.

The main aim of this investigation is to understand the feasibility of challenging scientific cases, but also to make quantitative predictions on the astrometric and photometric capabilities of an ELTcam, thus preparing the scientific community to the new ELT era (see also Fiorentino et al. 2017). The paper is structured as follows. In Section 2, we first introduce the *N*-body simulations used to create two cluster models, with and without an IMBH in the centre. We then describe how the mock ELTcam images of our simulated target are obtained in Section 3. Data reduction is described in Section 4. In Sections 5 and 6, we report the analysis of both photometry and astrometry and discuss the obtained performance and their impact on scientific results. Final remarks close the paper.

2 *N*-BODY SIMULATIONS OF R136

In this paper, as an input of our experiment we use direct *N*-body simulations of an R136-like cluster. To run the simulations, we use a new version of the direct summation *N*-body code HIGPUS (Capuzzo-Dolcetta & Spera 2013; Capuzzo-Dolcetta, Spera & Punzo 2013; Spera, in preparation). HIGPUS implements a Hermite sixth-order integration method (Nitadori & Makino 2008) with block time-steps (Aarseth 2003) and makes use of OpenCL to run on different computing architectures. For this paper, we have also included in HIGPUS the new AVX-512 instructions to effectively run our simulations on the latest Intel CPUs and on the new Intel Xeon Phi (Knights Landing) manycore processors.[4] We sampled two *N*-body models of an R136-like cluster. One model does not include an IMBH, while the other model contains a central IMBH of mass $10^4 \, M_\odot$.

Both models include $N = 100\,000$ stars, whose masses are distributed according to a Kroupa (2001) mass function in a range between 0.1 and 150 $M_\odot$. This implies that the initial mass of the cluster is $M_{cl} \simeq 60\,000 \, M_\odot$. Although stellar evolution, and in particular the fraction of binary systems, can have a strong impact on the cluster dynamics as recently detailed by Khorrami et al. (2016 and references therein), in our *N*-body simulations we did not account for it. This is because the main goal of this paper is to quantitate the precision and the accuracy we will obtain in dealing with future AO data and R136 is only taken as a suitable target for these observations.

The initial positions and velocities of stars are sampled from a King (1966) distribution with central dimensionless potential $W_0 = 9.0$ and King's core radius $r_c = 0.10$ pc, corresponding to an initial half-mass radius $r_{hm} = 2.9$ pc (Portegies Zwart, McMillan & Gieles 2010). Since this parameter evolves with time (see Khorrami

---

[1]For sky coverage is intended the portion of the sky including enough NGSs to perform AO observations.

[2]See also http://wwwmaory.oabo.inaf.it/wp-content/uploads/2016/11/E-M AO-000-INA-TNO-001_02.pdf.

[3]The Strehl ratio is used to measure the image quality of an optical system. It is defined as the ratio between the maximum of the PSF of the optical system and the maximum of its ideal diffraction pattern.

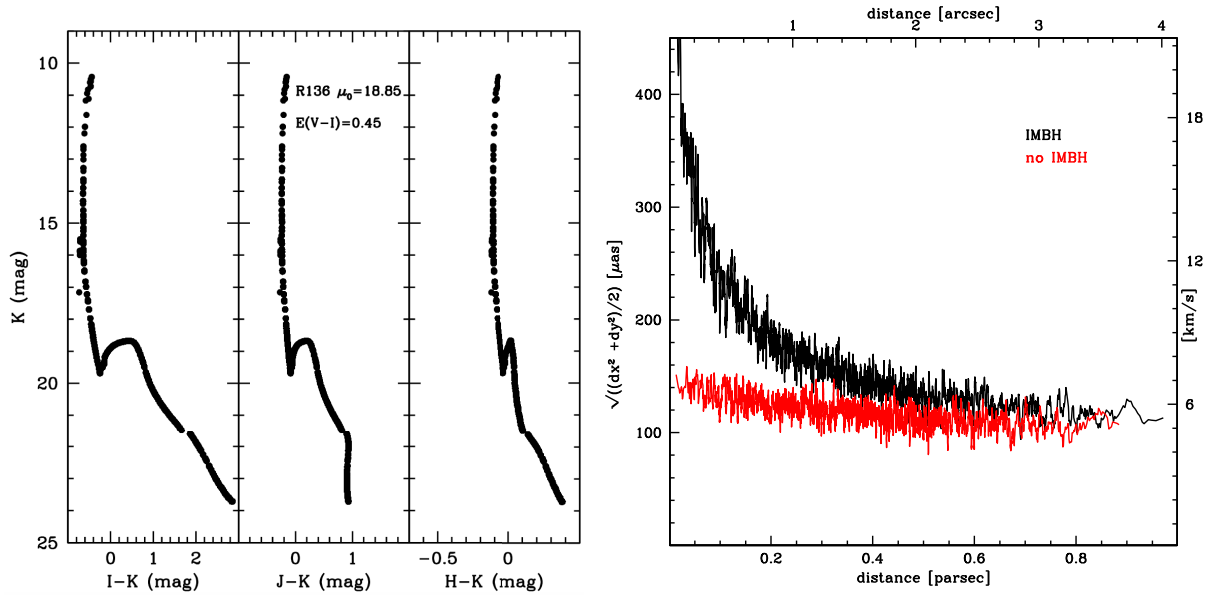[4]The details on the AVX-512 instructions can be found at https://software.i ntel.com/en-us/isa-extensions.

Figure 1. On the left, simulated *I–K*, *J–K*, and *H–K* CMDs are shown to highlight the colour sensitivity of the different filter combinations. They have been derived using the Padova evolutionary tracks data base, see http://stev.oapd.inaf.it/cmd and references in the text. On the right, the running average of the cluster absolute proper motion as predicted in the presence (black) or not (red) of an IMBH in the cluster centre. A colour version is available online.

et al. 2016), we have verified that in our simplified model this assumption after 3 Myr still returns a reliable R136-like cluster. In our simulations, we use a very small softening parameter of $\sim$4 $R_\odot$. This implies that gravitational forces are smoothed only inside this very small radius, similar to the physical radius of stars. Hence, binaries are allowed to form in our simulations. Furthermore, we do not include primordial binaries. Both our star cluster models start from virial equilibrium and have been evolved for $\sim$3 Myr. Two snapshots for each model have been considered, they are spaced by 5 yr, to simulate realistic observations at two epochs to estimate relative proper motions of individual stars.

To transform the *N*-body particles into observable stars, we have associated magnitudes in the desired photometric bands (*IJHK*) to each star, extracting them from an isochrone of age = 3 Myr and metallicity [M/H] = −0.35. We have used Padua stellar evolutionary models (Bressan et al. 2012; Tang et al. 2014; Chen et al. 2015; Marigo et al. 2017).[5] We then transformed absolute magnitudes into apparent magnitudes assuming a distance modulus of 18.48 mag for the LMC (Inno et al. 2016) and the following values of extinction: $A_I \sim 1.0$; $A_J \sim 0.65$; $A_H \sim 0.375$, and $A_K \sim 0.25$ (De Marchi et al. 2016). The resulting colour–magnitude diagrams (CMDs) are shown in Fig. 1 (left-hand panels) and highlight the effect of the sensitivity to the temperature of the filter combination, where the various sequences are more cleanly separated by colours with wider wavelength baselines. As an example, the hook formed by pre-main-sequence (PMS) stars approaching the main sequence (MS) is about one mag in *I–K* filter and decreases significantly when observing with a redder filter combination: it becomes $\sim$0.1 mag in *H–K*. This means that this feature can be observed with *H* and *K* filters only if photometric errors are small enough (see Section 5.1), with a direct impact on our ability of determining stellar ages.

To have an idea of the IMBH influence on the global cluster proper motions we have derived the mean shift in position (over

the adopted 5 yr time baseline) as a function of the radial distance, see Fig. 1 (right-hand panel). Note that the simulated star cluster has a zero systemic velocity. We have plotted only stars in the 5 arcsec × 5 arcsec across the cluster centre (see next section). The plot shows the running mean of the total motion in the plane of the sky, obtained by moving a bin forced to contain 40 stars from the centre of the cluster outwards, with step of five stars. The cluster centre has been estimated by using the stellar density functions of the stars in the *x* and *y* directions. The sphere of influence for an IMBH of 10^4 $M_\odot$ is expected to have a radius of about 1 pc ($r_{\rm inf} = G\, m_{\rm IMBH}/\sigma_{\rm cl}^2$, where $m_{\rm IMBH}$ is the IMBH mass and $\sigma_{\rm cl}$ is the central velocity dispersion of the star cluster), i.e. four arcsec at the distance of the LMC. To give an idea of the challenge inherent to the detection of this subtle effect, the difference between the two radial profiles at $R = 1$ arcsec is $\sim$50 μas in 5 yr, corresponding to $\simeq$2 km s^{-1} (see Section 6.1).

The influence radius is defined as the radius at which the contribution of the IMBH to the gravitational potential equals the total contribution of the other stars. Hence, we expect that the stars inside the influence radius are bound to the black hole and their motion is affected by the IMBH mass more significantly than by the other stars. This is what we see from the right-hand panel of Fig. 1: with a central IMBH, the 2D velocity grows more and more inside the influence radius with respect to the cluster without IMBH. Actually, a similar trend can be observed if the central mass of 10^4 $M_\odot$ is due to a very compact cluster of dark objects (such as stellar mass black holes), as recently shown by Zocchi, Gieles & Hénault-Brunet (2019). We do not investigate this case here, but it is worth mentioning that a compact cluster of dark objects (if it can stay in equilibrium for a long enough time-scale to observe its dynamical imprint) would be almost as interesting as a single IMBH from the gravitational wave perspective. Another physical ingredient that might compete with the IMBH's dynamical effect is the presence of binary stars. Our simulations do not contain any primordial binary, but binaries do form dynamically. The trend shown in our Fig. 1 is broadly consistent with the results obtained by other authors
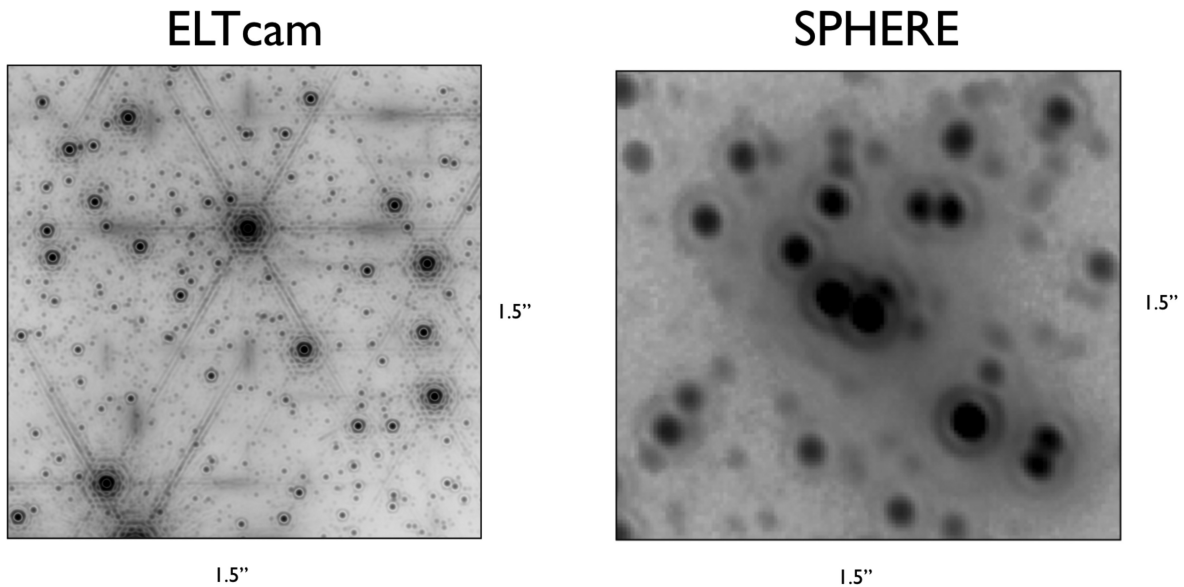
[5]http://stev.oapd.inaf.it/cgi-bin/cmd

ELTcam

SPHERE

Figure 2. Zoom on the cluster centre using the simulated SCAO *K*-band image (left) and a real one (right) of the centre of R136 taken with IRDIS/SPHERE at VLT (Khorrami et al. 2017a, b). The ELT simulated image is representing the IMBH case.

with similar simulations, which do not include primordial binaries but allow binaries to form dynamically (e.g. Baumgardt 2017; Baumgardt et al. 2019). These previous simulations also include stellar evolution, which is not implemented in our simulations. However, stellar evolution should not affect the velocity profile. Moreover, we stress that the goal of this paper is to predict whether or not ELT will be able to unveil an IMBH in a massive young star cluster by looking at stellar proper motions: producing a perfect *N*-body model of 30 Doradus is beyond our scope.

3 ELTCAM MOCK IMAGES

We have created a set of mock images of the star cluster using an ideal ELTcam defined as the high-resolution imager MICADO (Davies et al. 2016) fed by MAORY (Diolaiti 2016), in their current phase B designs. MICADO imager will have at disposal a large set of filters including classical *I*, *J*, *H*, and *K_s* broad-band filters. The two pixel scales available will be 1.5 and 4 mas, corresponding to FoV of 18.9 arcsec × 18.9 arcsec or 50.5 arcsec × 50.5 arcsec. Considering the high spatial resolution needed for our science case, we will use the 1.5 mas pixel scale. In fact, we need to explore the first few arcseconds of the cluster centre at the LMC distance, thus our simulation will be limited to the central 5 arcsec × 5 arcsec. The simulation of a small FoV is convenient to minimize the time spent in computation and data reduction. Furthermore, this choice is appropriate to assume a constant PSF across the FoV, as we will discuss later.

MAORY is supposed to work in two modes: (1) with a single natural guide star (SCAO, with $R \lesssim 15$ mag); (2) with an asterism of three NGS (with $H \lesssim 19$ mag)[6] plus six laser guide stars (MCAO). This latter mode will provide less extreme performances in terms of SR, but will ensure much higher sky coverage with respect to SCAO. Since, as said, the selection of suitable NGSs is not an issue for our target, both kind of observing modes will

be possible at the top of their performances, and therefore have been simulated so. Two grids of PSFs have been built using an 'ad hoc' End to End code (Arcidiacono et al. 2018) assuming median seeing conditions at the relevant site, as provided by ESO (0.57 arcsec in *I* band). The SR variation across the entire FoV is of ~70 per cent in SCAO and ~10 per cent in MCAO, however this decreases significantly to ~10 per cent and less than 1 per cent, respectively, in the first central arcseconds. Thus, our assumption of a constant PSF across the simulated 5 arcsec × 5 arcsec FoV may be not fully guaranteed by the SCAO technique. However, it should be a reasonable approximation for MCAO data, as proven on the sky by current instrumentation mounted at the 8-m class of telescopes (Monelli et al. 2015; Fiorentino et al. 2016; Massari et al. 2016a, b). We remind here that by assuming a constant PSF across the FoV we do not make any interpolation across the given PSF grid thus avoiding to introduce spurious trends in the results.

Using as key ingredients the above current phase-B instrument performance, we have simulated the images using an IDL code developed within the MAORY consortium and available upon request. The assumed telescope diameter is 39.146 m. The adopted filter profiles are those provided by the MICADO consortium. A properly scaled PSF was added to the mock image for any individual star contained in the simulated catalogue. Then we added background, dark current, and noise (photon and read-out noise). The total integration time is fixed at 20 min on target and the total image is assumed to be the sum of multiple single exposures of 1 min. For this total integration time a limiting magnitude in *K* band of about 24 mag is expected, this corresponds to stellar masses down to 0.1 $M_\odot$. A background image is simulated and subtracted from the image itself, to simulate a typical infrared observation.

As an example of the simulations we have obtained and to highlight the ELT potential, we propose a comparison with the best images ever taken of the centre of R136 cluster (see Fig. 2). The real image was taken in *K_s* using the extreme AO of SPHERE/IRDIS at VLT (see Khorrami et al. 2017a, b). The zoomed region is of 1.5 arcsec × 1.5 arcsec FoV. By a simple inspection of these images, it is already clear that ELT will allow us to make

---

[6] We note that magnitudes may be fainter than this limit when brighter NGSs are also included in the asterism.
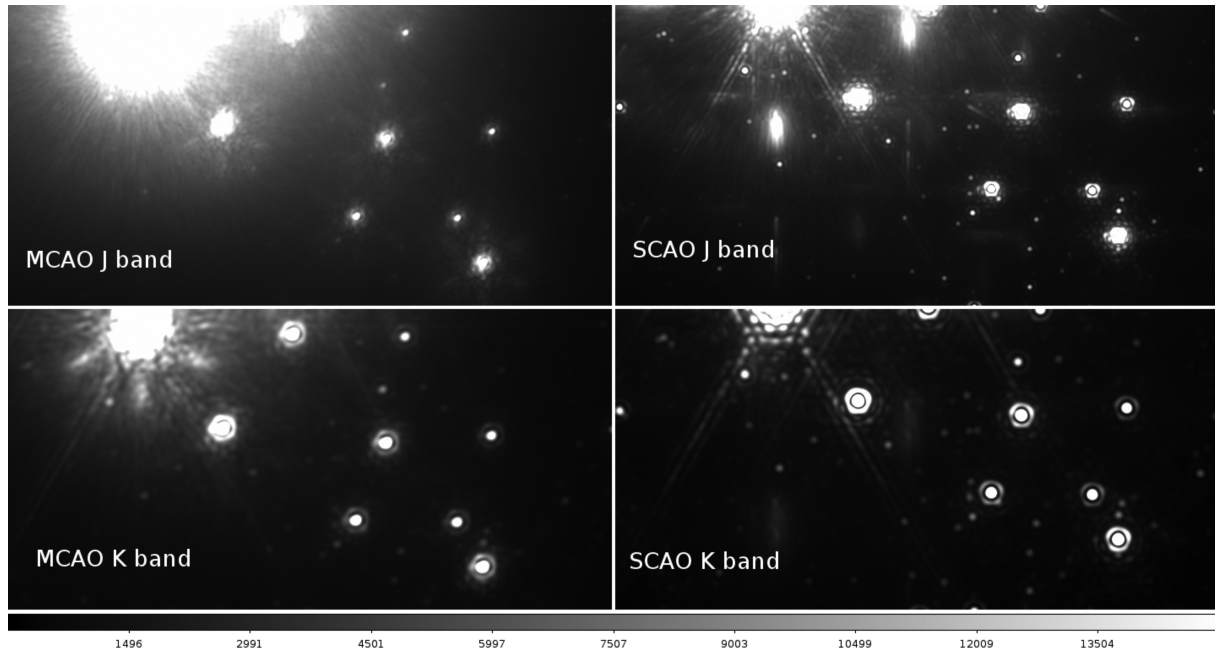
Figure 3. Zoom on some simulated cluster images using MCAO (left) and SCAO (right) modes for the model with the IMBH. *J* (top) and *K* (bottom) filters are shown. The FoV is 0.8 arcsec × 0.5 arcsec.

deeper analyses of the R136 cluster centre, as detailed in the following.

The final product of the full set of simulations consists of 32 images: 2 AO modes × 4 filters (*I*, *J*, *H*, and *K*) × 2 epochs × 2 cluster models, with and without the central IMBH. A few more examples of the simulated images are shown in Fig. 3 for *J* (top panels) and *K* (bottom panels) bands in SCAO (right-hand panels) and MCAO (left-hand panels) modes. We further zoom on (0.8 arcsec × 0.5 arcsec FoV) the images to highlight some of the PSF structures. In particular, in the SCAO case, the spiders coming from the telescope pupil together with the waffle modes introduced by the sensitivity of the wavefront sensor are well evident. In the PSF of MCAO images the effects of telescope spiders appear together with spots corresponding to the laser guide star asterism (in particular in *K* band). In *K* band, the diffraction limited core is well pronounced and evident in both SCAO and MCAO images.

4 DATA REDUCTION

We have used the suite of programs DAOPHOT/ALLSTAR (Stetson 1987, 1994) to perform both photometry and astrometry on all the simulated images. Although written to deal with seeing-limited images, DAOPHOT is known to perform well also in the DL regime (see e.g. Monelli et al. 2015; Saracino et al. 2015; Turri et al. 2015; Dalessandro et al. 2016; Fiorentino et al. 2016; Massari et al. 2016a, b; Monty et al. 2018, for applications to real AO images).

To have a realistic approach to data reduction, we have modelled the PSF using bright stars on the simulated images, thus not exploiting the a priori knowledge of the PSF. In particular, we have selected about 50 stars distributed across the FoV. We have excluded the very bright and contaminated stars. We highlight that we have not devoted a significant effort to properly model the PSF across the FoV, in this sense our analysis can be considered conservative. Images were searched for intensity peaks $\geq \sigma$ above the noise using

ALLSTAR. The final ALLSTAR star lists for each filter were cross-matched using CataXCorr.[7] We included in the match the original stellar inputs (magnitudes and positions), to test the performances of the observations + data reduction process (see Sections 5.1 and 6.1).

5 PHOTOMETRIC ANALYSIS

5.1 Photometric accuracy and precision

One of the goals of this paper is to quantify the photometric accuracy and precision expected by an ELTcam, on the basis of our present knowledge of the system.

The *photometric accuracy* is available by definition since we know exactly the stellar fluxes injected in the simulated images and we can compare them with those 'measured' through the PSF photometry (see Fig. 4). In this figure, the typical error distribution with increasing dispersion towards fainter magnitude is shown for all considered bands. It can be noticed also a small asymmetry towards the negative values when moving to faint magnitudes, which is due to blended sources (see Schreiber et al. 2014, for details). The limiting magnitude (at fixed exposure time) decreases when moving from longer to shorter wavelengths, due to the corresponding decrease of the AO performance. *H* and *K* bands show a similar behaviour. This general trend is similar in both SCAO and MCAO photometry, however MCAO reaches systematically brighter limiting magnitudes, again because of the lower SR with respect to SCAO.

Concerning the *photometric precision* that measures the reproducibility of our photometry, in principle we should repeat the experiment several times, re-doing image simulations and re-performing photometry. To save computational and data-reduction time, we decided to use, as a good indicator of the photometric

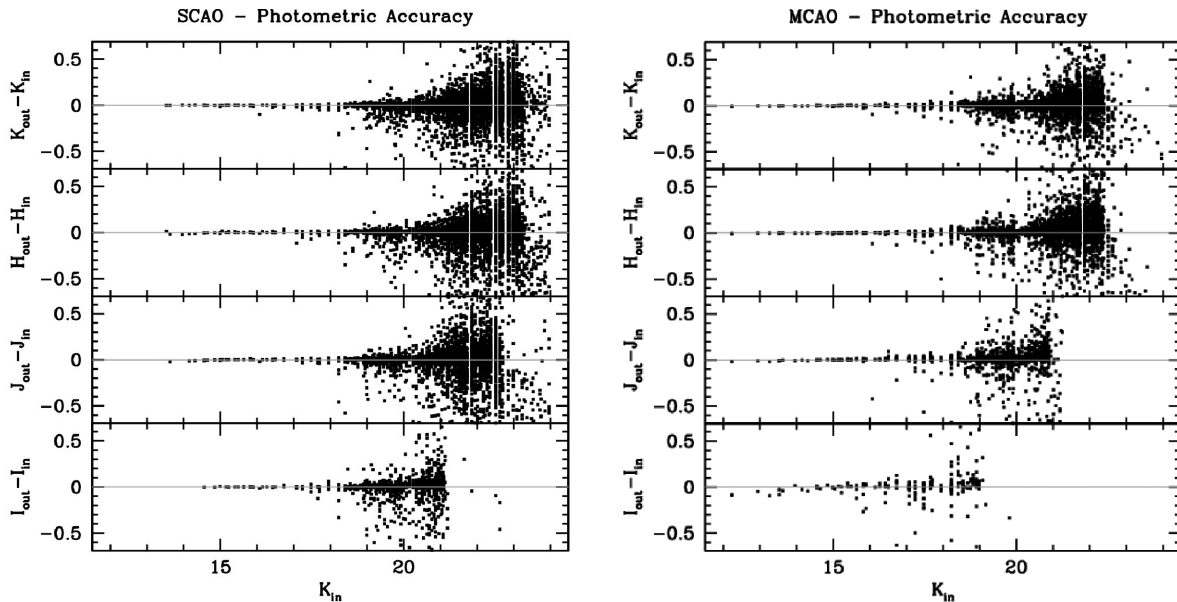[7]Developed by P. Montegriffo at INAF-OAS.

Figure 4. Expected photometric accuracy, differences between output (detected) and input magnitudes, for SCAO (left) and MCAO (right) modes in *I, J, H,* and *K* filters as labelled in each panel.

precision for each star, the difference between the two magnitudes obtained at two different epochs, shown in Fig. 5.

Our results are summarized in Table 1 where the mean magnitude difference and their standard deviations are listed. They have been obtained with a 3σ rejection after an iterative procedure of 20 steps. It is notable that the accuracy and the precision that can be reached in *K* band is of the order of millimag down to $K \sim 18.0$ mag and to 21.0 mag for MCAO and SCAO, respectively. These photometric accuracy and precision values may be useful to have an idea of the ELTcam performance for other resolved stellar population studies (e.g. those listed in Fiorentino et al. 2017).

A systematic in the accuracy, increasing at fainter magnitudes, can be appreciated looking at the mean magnitude differences in Table 1, particularly in the MCAO mode. The output magnitudes are slightly fainter that the input ones. The effect may reach an amplitude of $\simeq 0.05$ mag at the limiting magnitude and is observed in all the considered passbands. We did not investigate the origin of this effect; a reasonable hypothesis is that it can be related to the estimate of the residual background that is performed by DAOPHOT on the sky-subtracted images or, possibly, to inadequacy of the simple PSF model we adopted. This effect is not seen when precision is considered.

The accuracy and precision measured here for bright stars are compliant with the top level requirements of ELTcam, that are defined for isolated stars measured at high signal-to-noise ratio.

5.2 Colour–magnitude diagrams

In this section we present the first scientific output of the simulated photometry, i.e. the CMDs that can be used to infer age, distance, and metallicity of the cluster. In Fig. 6, we have shown both the input (red dots) and output (black dots) colours and magnitude of the stars, to allow a direct comparison.

The output CMDs nicely reproduce all the input features in all passbands, down to the limiting magnitude. In this sense, the photometric performance is very satisfactory (see below, for a comparison with *HST* photometry). To quantify the quality of

our photometry and to highlight the sensitivity of the colour to the temperature, we select one feature in the CMD and we try to measure it using the different colour combination. We select the colour extension of the typical hook formed by PMS stars approaching the MS (almost a vertical line), the so-called MS cut-off (MSCO). This feature, located at magnitudes $19.5 \leq K \leq 20.2$, has the following theoretical colour extensions $I-K = 1.08 \pm 0.04$, $J-K = 0.48 \pm 0.02$, and $H-K = 0.08 \pm 0.005$ mag. These numbers are the median colours and the corresponding standard deviations in the semi-interquartile range. We then measure these colours from the derived CMDs and we obtain the following results depending on the AO mode: *SCAO)* $I-K = 1.08 \pm 0.07$, $J-K = 0.48 \pm 0.02$, and $H-K = 0.09 \pm 0.01$; *MCAO)* $J-K = 0.487 \pm 0.04$ and $H-K = 0.08 \pm 0.02$. These numbers give us the idea of the extremely good photometric accuracy and precision we can reach with both modes. Our ability in identifying the MSCO provides us a robust and well populated observable to accurately determine the cluster age. In fact, we note here that ages of young star clusters are often difficult to measure adopting the classical stellar clock (the MS turn-off), which is barely populated.

In general, SCAO CMDs are, as expected, deeper and cleaner than MCAO ones. The full PMS including the very faint stars down to 23.5 mag (corresponding to masses of ~ 0.15 M$_\odot$) and with errors of ~ 0.1 mag is only visible in the $H-K$ CMD taken with SCAO. The MCAO results are still good with the exception of the $I-K$ filter combination. Although the MCAO $H-K$ CMD is less deep, it reaches photometric errors of the order of 0.1 mag at $K \sim 21$–22 mag, thus still impressive when compared with current results from the Tarantula survey (Sabbi et al. 2016). This survey observed the Tarantula star-forming region of the LMC by using the WFC3 infrared channel onboard *HST*, where a particular attention has been devoted to star clusters as R136. In their study, Sabbi et al. (2016) show a CMD for the stars within 1 pc from the centre of R136, this radial distance fully includes our simulated FoV. From their diagram it is clear that the 'PMS hook' cannot be detected, it can be barely seen as a change in the slope between MS and PMS stars. R136 cluster centre has been hardly explored
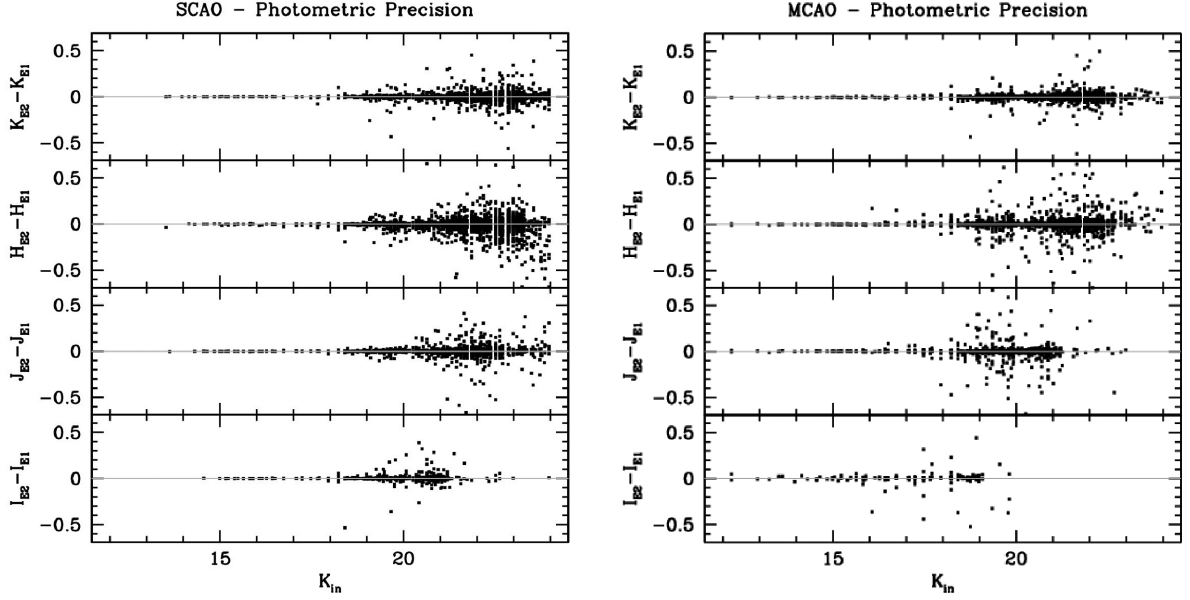
Figure 5. Estimate of the photometric precision for SCAO (left) and MCAO (right) modes in *I*, *J*, *H*, and *K* filters as labelled in each panel. This has been obtained using for each model and photometric band the two different epochs (0 and 5 yr).

Table 1. Photometric accuracy and precision for both AO modes.

| K range (mag)	N_K	$\langle\Delta_K\rangle$ (mag)	σ_K (mag)	N_H	$\langle\Delta_H\rangle$ (mag)	σ_H (mag)	N_J	$\langle\Delta_J\rangle$ (mag)	σ_J (mag)	N_I	$\langle\Delta_I\rangle$ (mag)	σ_I (mag)
					Accuracy MCAO							
12–16	36	0.0000	0.0015	39	0.0000	0.0023	41	0.0000	0.0077	36	− 0.0158	0.0419
16–18	90	0.0038	0.0041	94	0.0048	0.0068	96	0.0120	0.0134	72	− 0.0049	0.0621
18–19	155	0.0066	0.0146	155	0.0079	0.0182	158	0.0064	0.0345	65	0.0508	0.1013
19–20	398	0.0056	0.0270	382	0.0059	0.0268	372	0.0137	0.0414	–	–	–
20–21	373	0.0080	0.0579	356	0.0114	0.0553	291	0.0569	0.1042	–	–	–
21–22	1244	0.0306	0.1112	1213	0.0397	0.1177	–	–	–	–	–	–
22–23	592	0.0465	0.1313	590	0.0441	0.1764	–	–	–	–	–	–
					Accuracy SCAO							
12–16	33	0.0000	0.0010	36	0.0000	0.0079	33	0.0000	0.0045	26	0.0000	0.0020
16–18	93	0.0013	0.0024	102	0.0043	0.0046	93	0.0046	0.0017	93	0.0010	0.0020
18–19	169	0.0023	0.0081	166	0.0061	0.0063	156	0.0067	0.0062	169	0.0008	0.0124
19–20	408	0.0041	0.0154	411	0.0065	0.0119	411	0.0091	0.0140	416	0.0036	0.0195
20–21	435	− 0.0033	0.0457	433	0.0028	0.0394	425	0.0084	0.0554	367	0.0214	0.0645
21–22	1549	0.0048	0.0770	1478	0.0073	0.0648	1454	0.0196	0.1172	–	–	–
22–23	2416	0.0358	0.0983	2358	0.0302	0.0968	1228	0.0277	0.1709	–	–	–
					Precision MCAO							
12–16	39	0.0001	0.0008	41	− 0.0002	0.0030	39	0.0012	0.0029	38	0.0031	0.0222
16–18	93	0.0000	0.0011	90	0.0013	0.0033	95	0.0000	0.0047	60	0.0087	0.0049
18–19	148	− 0.0005	0.0018	147	0.0024	0.0063	137	− 0.0020	0.0024	65	0.0097	0.0111
19–20	396	0.0000	0.0028	367	0.0016	0.0058	357	− 0.0022	0.0042	–	–	–
20–21	369	0.0000	0.0053	342	0.0011	0.0059	290	− 0.0025	0.0136	–	–	–
21–22	1240	− 0.0006	0.0105	1160	0.0015	0.0122	–	–	–	–	–	–
22–23	615	0.0009	0.0152	556	0.0026	0.0203	–	–	–	–	–	–
					Precision SCAO							
12–16	36	− 0.0001	0.0008	28	0.0006	0.0012	30	− 0.0003	0.0004	25	− 0.0003	0.0015
16–18	99	− 0.0005	0.0008	103	− 0.0006	0.0038	104	− 0.0003	0.0006	99	0.0001	0.0008
18–19	165	− 0.0008	0.0016	176	− 0.0010	0.0041	150	− 0.0002	0.0008	170	− 0.0002	0.0013
19–20	426	− 0.0008	0.0021	403	0.0000	0.0041	404	0.0000	0.0014	423	− 0.0002	0.0016
20–21	418	− 0.0011	0.0029	409	0.0009	0.0059	405	− 0.0002	0.0027	388	− 0.0003	0.0047
21–22	1515	− 0.0010	0.0056	1381	0.0018	0.0074	1469	− 0.0004	0.0066	–	–	–
22–23	2497	− 0.0070	0.0111	2260	0.0038	0.0131	1261	− 0.0006	0.0117	–	–	–
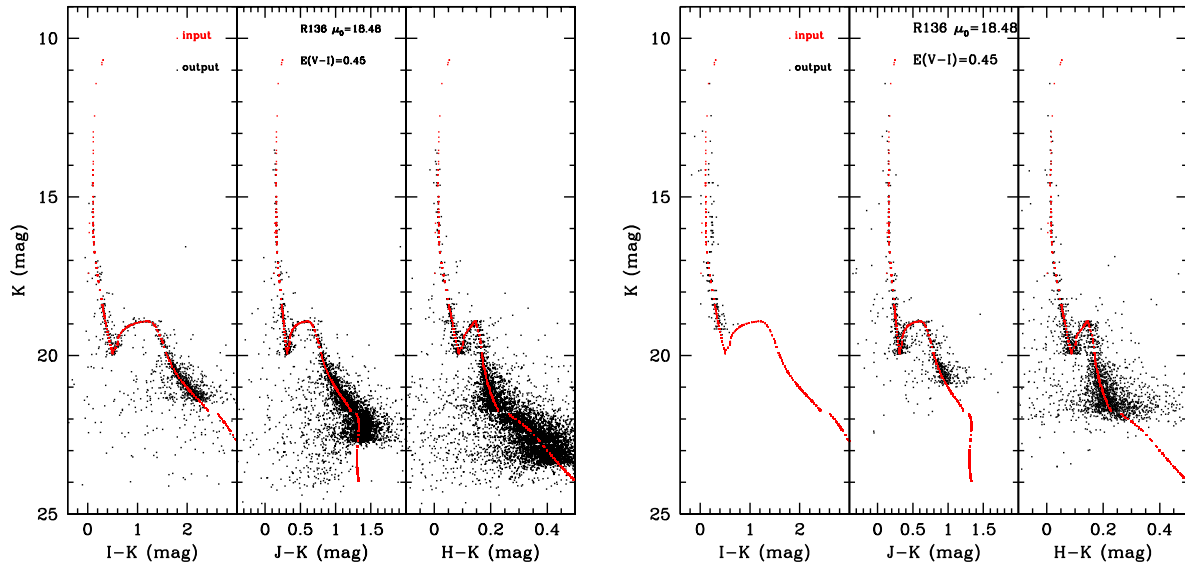
Figure 6. Comparison between the input *I–K*, *J–K*, and *H–K* CMDs (red dots) and the estimated ones (black dots) using SCAO (left) and MCAO (right) simulations. The model without the IMBH is shown, results for the model with IMBH do not show any difference. A colour version is available online.
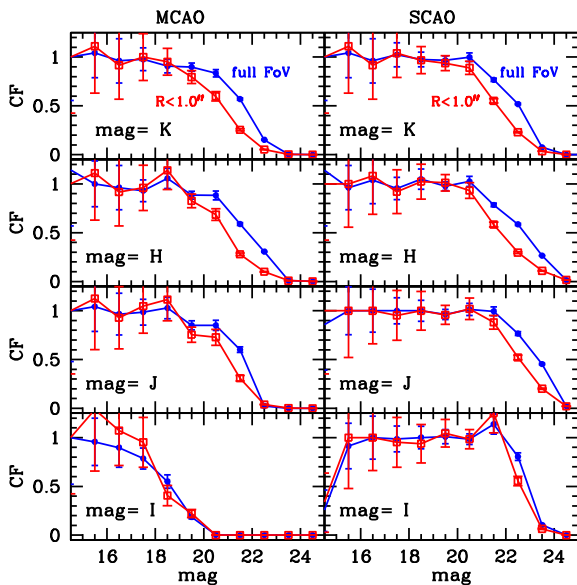

Figure 7. Completeness function derived by comparing input versus detected sources plotted against the *K*-band magnitude for each considered filter and for each AO mode. Blue and red lines indicate all the simulated stars and only those within 1 arcsec of radius from the cluster centre, respectively. A colour version is available online.

using space-based data (Sabbi et al. 2016), whereas a better view has been possible with the current extreme AO observations at VLT (IRDIS/SPHERE Khorrami et al. 2017a, b). MAORY + MICADO will open a new window on the cluster centre by allowing a detailed analysis of its central stellar population and radial distribution.

In Fig. 7, we show the completeness functions for each filter and AO mode, derived using the ratio between output and input stellar numbers per magnitude bin for all the stars (blue lines) and only for those within 1 arcsec from the centre (red lines). As expected, these

ratios approach unity at bright magnitudes and decrease going to the faintest magnitudes. Few values larger than one can be easily explained by blended sources. For reference, the magnitude where a completeness of ∼50 per cent is reached in the various cases is: $K_{SCAO}, H_{SCAO} \sim 22.5, J_{SCAO} \sim 23.5, I_{SCAO} \sim 23; K_{MCAO}, H_{MCAO}, J_{MCAO} \sim 21.5, I_{MCAO} \sim 18.5$.

In the assumption of a constant PSF across the small considered FoV, the SR is much higher in SCAO mode than in MCAO, a factor of ∼2, 2, 6, and 45 larger for *K*, *H*, *J*, and *I*, respectively. Thus, SCAO will perform much better than MCAO by construction, on this small FoV. In *I* band, the MCAO performance drops down due to the very low energy concentration in the diffraction limited core, i.e. SR = 0.05. To highlight the effect on completeness of the exquisite spatial resolution of our simulated observations we also show in Fig. 7 the completeness function in the very centre of R136 (stars within a radius of 1 arcsec). It can be appreciated that it is hardly distinguishable from that of the whole sample.

6 ASTROMETRIC ANALYSIS

6.1 Astrometric accuracy and precision

In this section we discuss the astrometric performance expected for an ELTcam. As for the photometric case, we are able to estimate directly the *astrometric accuracy* since we have at disposal the injected and measured positions in both *x* and *y* directions. In the following we report the analysis only for the *x*-axis, since they are indistinguishable from those obtained for *y*-axis. These are shown in Fig. 8 and Table 2 as a function of bins of *K* magnitude. We note that all the values reported in Tables 2 and 3 have passed a 3σ rejection criterion of 20 steps. By an inspection of Fig. 8, it can be seen that the performance in *H* and *K* bands is very good and similar in the two bands, whereas it worsens in the *J* and *I* band, in particular for the MCAO mode. It is important to notice that the astrometric accuracy reached in *I* band with SCAO is comparable or even better than the one obtained with other filters for *K* ≤ 21 mag, however it drops to zero very rapidly going to fainter magnitudes.
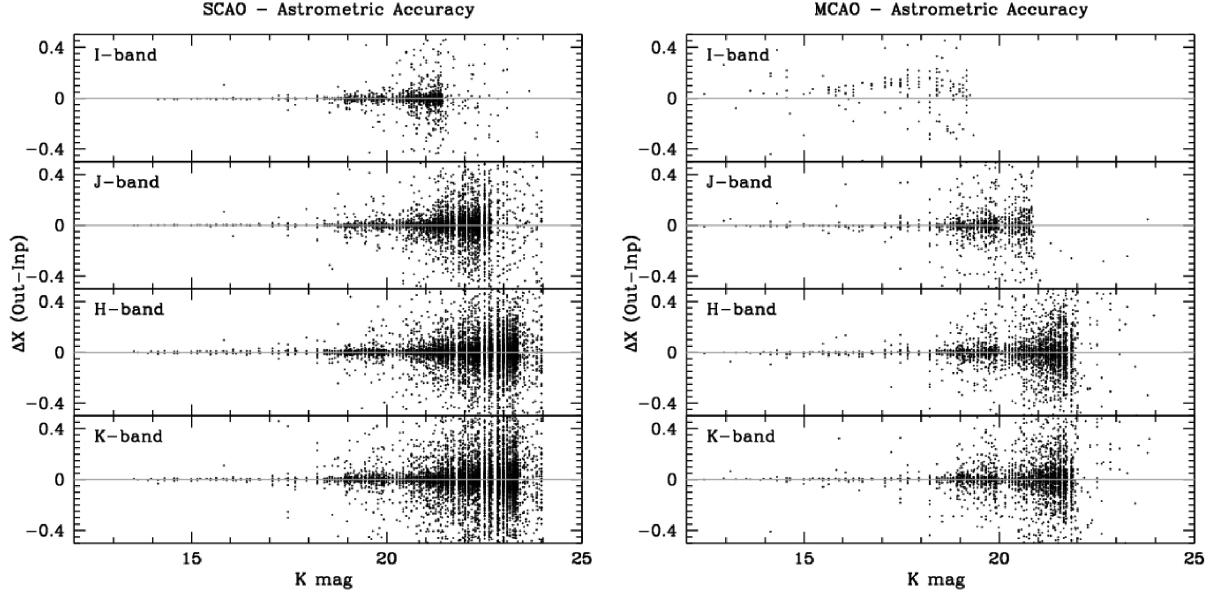
Figure 8. Differences between input and output star positions in pixels in the four considered passbands. These allow us to estimate the astrometric accuracy for SCAO (left) and MCAO (right) modes.

Table 2. Astrometric accuracy for both AO modes. Note that $\langle\Delta x\rangle$ are subtracted by a constant value due to the not perfectly centred PSF functions used to inject the stars into the images. The PSF centre changes with the photometric band.

K range (mag)	N_K	$\langle\Delta x_K\rangle$ (μas)	σ_K (μas)	N_H	$\langle\Delta x_H\rangle$ (μas)	σ_H (μas)	N_J	$\langle\Delta x_J\rangle$ (μas)	σ_J (μas)	N_I	$\langle\Delta x_I\rangle$ (μas)	σ_I (μas)
						MCAO						
12–16	37	0.0	7.0	39	0.0	10.6	37	0.0	4.1	36	0	71.9
16–18	96	4.7	23.3	96	0.5	19.5	91	−4.7	15.4	76	15.8	248
18–19	156	−0.4	53.3	155	6.2	48.5	154	0.4	74.8	75	57.6	288
19–20	397	−0.2	96.1	383	−1.1	81.5	372	−3.9	115.5	9	−646.9	1428
20–21	390	29.0	263.4	369	29.5	206.5	294	39.8	323.3	–	–	–
21–22	1296	4.4	356.3	1236	16.7	355.3	–	–	–	–	–	–
22–23	662	4.4	445.0	622	−2.6	488.5	–	–	–	–	–	–
						SCAO						
12–16	34	0.0	9.0	33	0.0	14.5	33	0.0	2.5	26	0.0	3.4
16–18	100	0.05	12.6	109	−4.4	25.6	98	0.0	3.4	105	0.5	4.2
18–19	156	0.8	16.7	174	−0.7	23.3	168	−0.4	7.5	172	1.8	9.2
19–20	418	1.5	44.9	425	−7.9	28.4	388	−1.0	11.1	428	0.8	14.0
20–21	389	−3.9	84.1	416	2.4	65.9	394	3.0	42.5	376	8.2	37.6
21–22	1470	−0.4	166	1456	0.4	106.7	1440	−5.4	109.5	–	–	–
22–23	2496	−2.1	256.6	2369	−2.2	149.4	1215	−0.1	164.6	–	–	–

In general, the *I*-band astrometric accuracy reached with SCAO in the bright magnitude range is very impressive since it is always better than 50 μas.[8] Presumably, in the analysed wavelength range, in the trade-off between worsening AO correction and squeezing the width of the DL PSF at shorter wavelengths, the second factor is prevailing.

Slightly worse performance are reached with MCAO, as expected. An astrometric accuracy higher than 50 μas is reached in this AO mode only in *H* and *K* bands and for stars brighter than $K \simeq 19.0$ mag. The results on the astrometric accuracy are summarized in Table 2.

To have an idea of the *astrometric precision*, without performing new image simulations, we decided to compare proper motions (PM) obtained from images in the two epochs in different passbands. In Fig. 9, we show the differences between the PMs estimated from *I*, *J*, and *H* images and those obtained from *K* images, taken as reference. The agreement between PMs measured in different passbands is excellent. These differences, summarized in Table 3, show dispersions around the mean always smaller than a dozen μas yr^{-1} for both modes. We highlight that our mock observations have been obtained using two epochs separated by 5 yr, thus to obtain astrometric precision in μas we need to multiply by five these results. This means that the top level requirement for MAORY and MICADO of precision better than 50 μas is fulfilled for the entire stellar magnitude range analysed. We highlight that when using the MCAO mode, *H* and *K* positions show a small zero-point of $\sim$2.5 μas yr^{-1}. It is difficult to assess the reasons why this happens;

---

[8] We recall here that 50 μas is the current top level requirement for astrometry with the current design of MAORY and MICADO.

Table 3. Proper motions precision for both AO modes.

K range (mag)	N_{HK}	$\langle \Delta x_{HK} \rangle$ (μas yr^{-1})	σ_{HK} (μas yr^{-1})	N_{JK}	$\langle \Delta x_{JK} \rangle$ (μas yr^{-1})	σ_{JK} (μas yr^{-1})	N_{IK}	$\langle \Delta x_{IK} \rangle$ (μas yr^{-1})	σ_{IK} (μas yr^{-1})
				MCAO					
12–16	45	2.8	0.9	47	−0.3	2.1	–	–	–
16–18	103	2.3	0.9	111	0.2	2.6	–	–	–
18–19	160	2.7	2.4	153	−1.1	2.9	–	–	–
19–20	477	2.3	3.6	469	−1.2	4.4	–	–	–
20–21	458	1.7	7.6	337	−1.6	10.9	–	–	–
21–22	1229	2.5	14.9	–	–	–	–	–	–
22–23	–	–	–	–	–	–	–	–	–
				SCAO					
12–16	43	−0.04	0.66	42	−0.3	1.49	28	0.07	0.66
16–18	100	−0.24	0.46	101	0.40	0.61	101	0.48	0.48
18–19	160	−0.14	1.00	161	0.13	1.56	149	0.56	0.89
19–20	485	−0.09	1.57	489	0.06	1.93	483	0.24	1.95
20–21	483	0.10	2.70	479	−0.31	3.12	479	−0.18	3.79
21–22	1653	−0.28	4.91	1648	−0.15	5.61	506	0.08	5.54
22–23	3078	−0.13	11.4	1833	0.28	10.8	–	–	–

Notes. We did not include MCAO results obtained using I and K combinations since they are based on few stars.
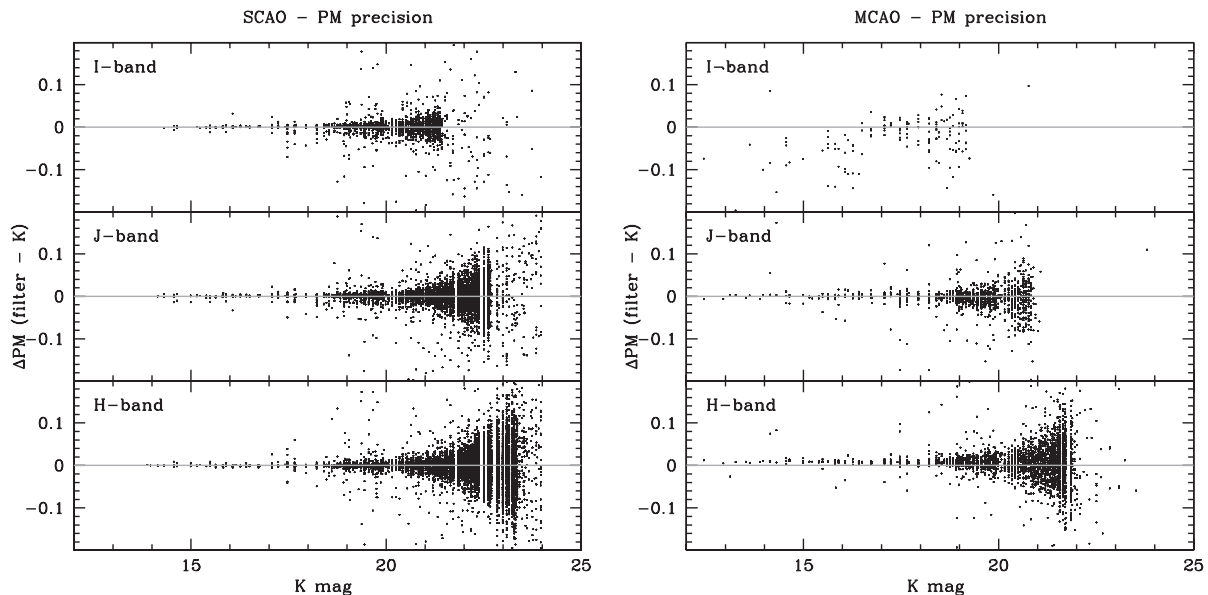

Figure 9. Differences between the output star positions in pixels in I, J, and H bands compared with those in K band, used as reference. These allow us to estimate the astrometric precision for SCAO (left) and MCAO (right) modes.

however we notice that this offset is within the uncertainty on the stellar centroid determination of ∼0.01 pixel expected when using DAOPHOT/ALLSTAR (Stetson 1987) to perform the PSF fitting.

6.2 Proper motions

In this section, we discuss the accuracy of PMs we derive from our images in the context of the science case of the detection of an IMBH at the centre of the considered star cluster. In practice, we want to verify if our astrometric accuracy is adequate to detect the difference in the velocity dispersion curve between the cluster models with and without IMBH.

In Fig. 10, we show the direct comparison between the simulated and observed radial distribution of the mean position shifts in 5 yr (analogously to Fig. 1), in the various passbands and for the

two considered AO modes. The signal from the central IMBH is successfully detected in our simulated observations in any passbands and in both modes, except for I-band observations in MCAO mode, where the bright limiting magnitude severely reduces the number of detected stars in the central region, making an adequate sampling of the velocity profile impossible. It is likely that this problem can be overcome with longer exposure times, but our experiment suggests that MCAO I-band observations are not the most efficient way to perform this kind of study.

It is important to note here that the key factors allowing us to achieve this challenging scientific goal are two: (1) the exquisite astrometric accuracy/precision, and (2) the extraordinary resolving power of the AO-assisted ELT, that makes possible to measure reliable positions for a large number of stars (down to very faint magnitudes) even in the innermost 0.2 arcsec of a dense star
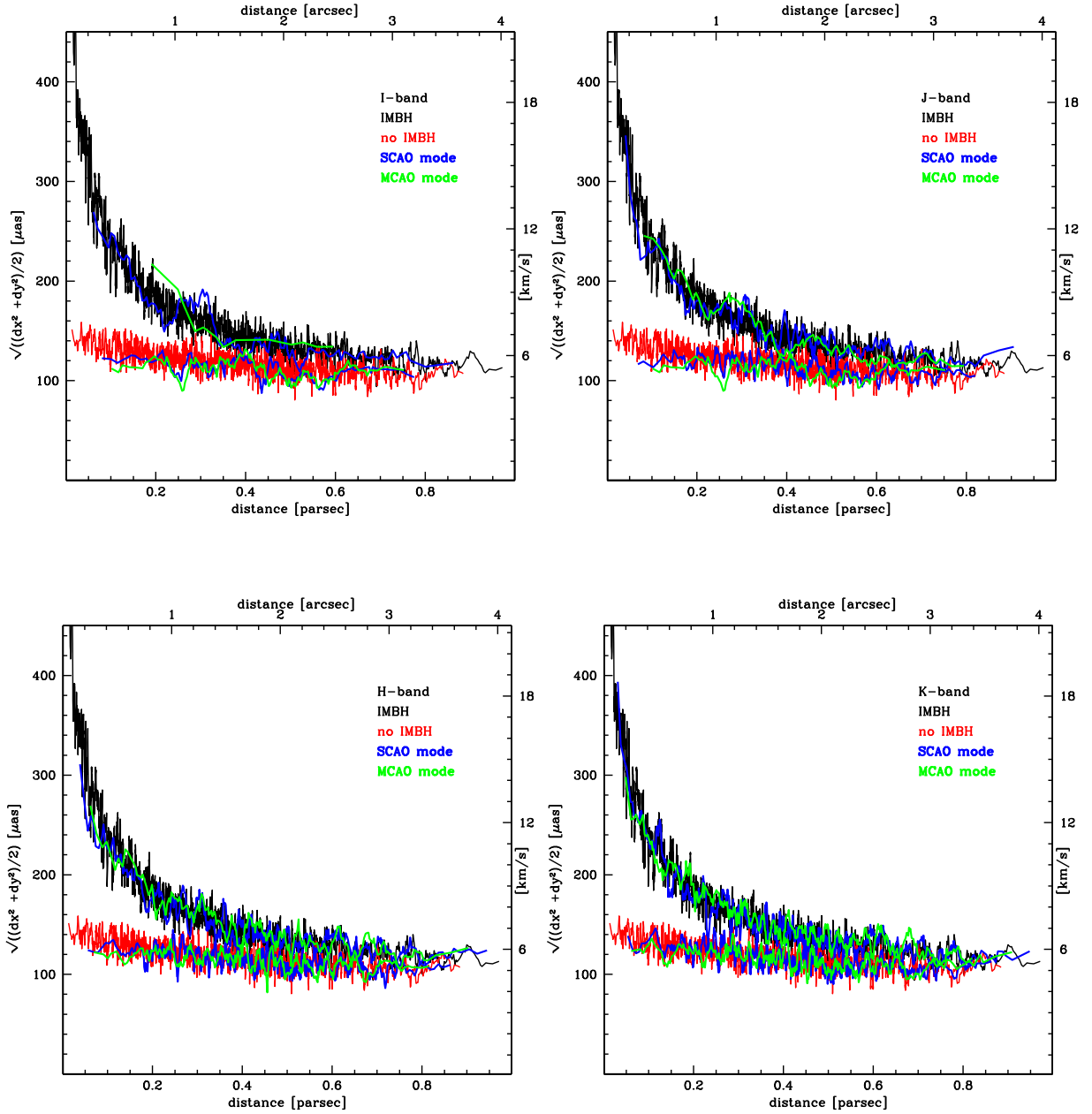
Figure 10. As in Fig. 1 (right-hand panel), we show the theoretical PMs of the two cluster models and we added the derived profiles by using both SCAO (blue) and MCAO (green) techniques. The photometric band is labelled in each panel. We note that the two snapshots are taken at 3 Myr, i.e. the age selected to simulate R136. A colour version is available online.

cluster in the LMC. This second factor is crucial to sample the velocity curve in the very small sphere of influence of the IMBH, a spatial resolution regime where ELTs are expected to have no competitors.

In Fig. 11, we show the same results for the MCAO mode and *K*-band images, in a form more readily linked to the common practice of the kinematics of star clusters, i.e. comparing the velocity dispersion curve of the model with the observed one. We adopted radial bins 1.0 arcsec wide, with the exception of the central arcsec that was divided in two bins to follow the steepening of the curve very close to the IMBH. The difference in quadrature between predicted and *measured* σ values in both directions are also plotted (bottom panels). The astrometric precision and accuracy reached by

our experiment are good enough to distinguish the two cases within the entire influence radius, i.e. ~ 4 arcsec for an IMBH mass of 10^4 M$_\odot$. In fact, the errors in our σ estimates are extremely small: ~ 10 μas yr^{-1} or 1–2 km s^{-1}.

In our paper, we consider only one IMBH of mass $m_{IMBH} = 10^4$ M$_\odot$. While the possible mass range of IMBHs in star clusters is still very uncertain (see e.g. Mapelli 2016), an IMBH mass of 10^4 M$_\odot$ in a star cluster of $\sim 10^5$ stars represents a robust upper limit to the mass of IMBHs formed by runaway collisions or by repeated mergers (see e.g. Arca Sedda et al. 2019). In addition, we wish to mention that a substantial fraction of primordial binaries would reduce the amount of mass segregation in a similar way to what an IMBH does (Pasquato et al. 2009; Khorrami et al. 2016). Hence, including
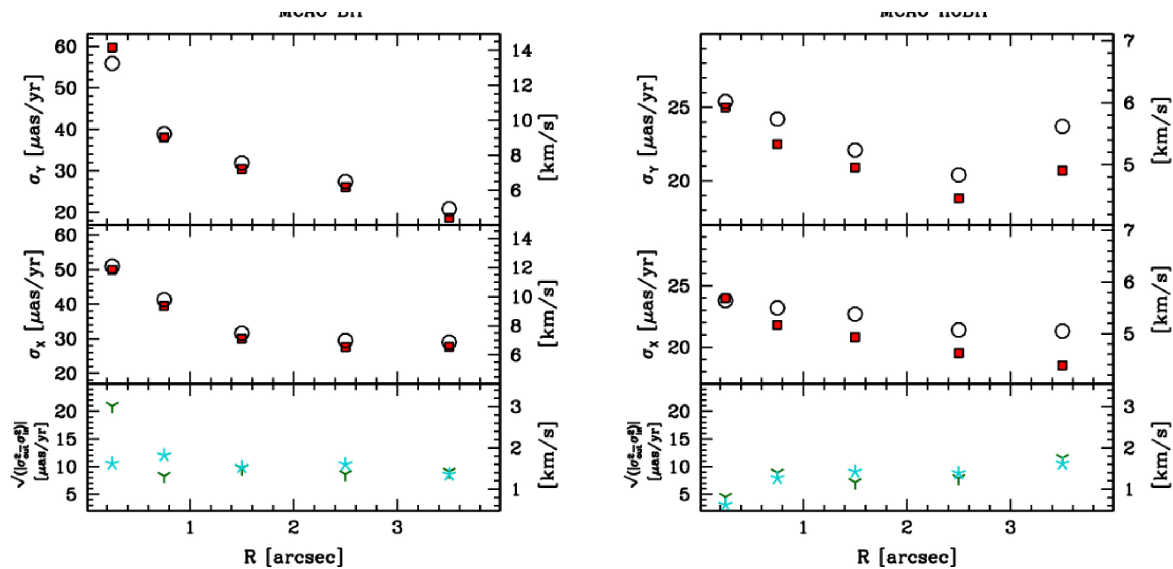
Figure 11. Velocity dispersion profiles of the simulated clusters, with (left-hand panels) and without (right-hand panels) central IMBH, in the *x*- (middle panels) and *y*- (upper panels) coordinates. The dispersions are estimated as straight standard deviations in radial bins of fixed width (hence with very different numbers of stars) from the original *N*-body models (red filled squares) and from the catalogues we obtained from simulated MCAO observations (open circles). The square root of the quadrature difference between the σ from the observations and from the model (lower panels, $\times$ symbols for σ_X and skeletal triangles for σ_Y) is an estimate of the observational error on the dispersion, that is consistently found to be $\simeq 10.0$ μas yr^{-1} = 2.0 km s^{-1}. Fluctuations around this mean value are due to shot noise associated with relatively underpopulated bins. A colour version is available online.

primordial binaries in the simulation without IMBH would make the global dynamical evolution of the star cluster without IMBH be more similar to the star cluster with the IMBH.

In this proof-of-concept paper, we have shown that IMBHs with mass $\geq 10^4$ M$_\odot$ can be detected by ELT to the distance of the LMC. In a follow-up study (Sabha et al., in preparation) we will estimate what is the minimum IMBH mass observable with ELTs in star clusters of different mass and at different distance (e.g. the Arches cluster close to the centre of the Milky Way).

7 FINAL REMARKS

In this paper, we have analysed the case of study of a young star cluster located in the LMC, e.g. R136. This target is interesting from a scientific and a technological point of view. The inner crowded regions of young clusters outside our Galaxy are not well studied and may contain important details on their formation and evolution. Furthermore, these star clusters are ideal candidates as birthplaces of IMBHs. From a technological point of view, the investigation of challenging astrometric and photometric targets can provide hints to drive the fine tuning of future ELT instrumentation.

We have analysed the behaviour of SCAO and MCAO in four wide-band filters, i.e. *I*, *J*, *H*, and *K* band. Our first result is that *H* and *K* bands perform very similarly for both photometric and astrometric goals, with *H* band being by construction less contaminated by the sky brightness. Photometric performance has been analysed in detail using the a priori knowledge on the stellar magnitude injected in the mock images. This experiment demonstrates excellent photometric accuracy and precision, down to the limiting magnitude, of the order of few hundredth- and few milli-mag, respectively.

We highlight the need to be very careful when analysing CMDs. In fact, the use of a pure infrared CMD (e.g. *K*, *H*–*K*) may reduce the sensitivity of the colour to the temperature by squeezing features that disappear even with the high level of photometric precision reached (see also Fiorentino et al. 2011; Schreiber et al. 2014).

Thus, although trivial, we suggest to pay particular attention when choosing the observing filters, that have to depend strictly on the desired science case.

Concerning astrometry, we have analysed the possible dynamical detection of an IMBH with mass $\sim 10^4$ M$_\odot$. The best astrometric performance is achieved in *H* and *K* bands (as shown in Fig. 10), that allow us to detect very faint stars (down to $K \sim 22$ and 24 mag with MCAO and SCAO, respectively) and to accurately measure their positions. We highlight that the IMBH mass chosen in our experiment is an upper limit to the current IMBH estimate. In a follow-up study (Sabha et al., in preparation), we will investigate what is the minimum IMBH mass that can be revealed by ELT in star clusters of different mass at different distances.

By taking advantage of the ELTcam mock images created for this experiment, we are also able to make some predictions on the SCAO and MCAO performance in terms of astrometry and photometry. The results are very impressive in particular concerning the astrometric capability of future telescopes, as shown in Tables 1–3. Given the current PSF simulations from the MAORY consortium, the astrometric top level requirement of 50 μas seems to be safely fulfilled.

We note that, as discussed along the paper, for this specific scientific case where an extreme astrometric performance in a small FoV is needed, SCAO mode provides the best performance. However, we need to take in mind that the presence of a bright star ($R \leq 15$) within the FoV (which is essential for SCAO mode) may severely limit the targets we can observe (i.e. the sky-coverage). Moreover, the presence of a bright star in the science image may decrease the photometric and astrometric quality of the measurements nearby the star used as guide. Finally, we remind that the SCAO performance adopted here could be overestimated since the assumption of a slowly varying PSF across the FoV is less robust than for the MCAO case. For the above reasons, observations with the MCAO mode may be often the only way to observe some targets. However, we have shown that the MCAO performance is

still very attractive and will allow us to explore, as an example, the crucial dynamical signature of an IMBH in a star cluster.

The study presented in this paper highlights the dramatic impact of future *big eyes* on challenging science cases. Today, the scientific community is required to devote some efforts in understanding the feasibility and in planning these future observations, since the ELT observing time will be very precious. In the future, our approach to make ELTmock observations may become the standard way in order to get regular observing time to these new facilities.

REFERENCES

Aarseth S. J., 2003, Gravitational N-Body Simulations. Cambridge Univ. Press, Cambridge, p. 430

Anderson J., King I. R., 2006, Technical Report, PSFs, Photometry, and Astronomy for the ACS/WFC. Instrument Science Report ACS 2006-01, p. 1

Arca Sedda M., Berczik P., Capuzzo-Dolcetta R., Fragione G., Sobolenko M., Spurzem R., 2019, MNRAS, 484, 520

Arcidiacono C. et al., 2018, in Close L. M., Schreiber L., Schmidt D., eds, Proc. SPIE Conf. Ser. Vol. 10703, Adaptive Optics Systems VI. SPIE, Bellingham, p. 107034I

Baumgardt H., 2017, MNRAS, 464, 2174

Baumgardt H. et al., 2019, MNRAS, 488, 5340

Boekholt T. C. N., Schleicher D. R. G., Fellhauer M., Klessen R. S., Reinoso B., Stutz A. M., Haemmerlé L., 2018, MNRAS, 476, 366

Bressan A., Marigo P., Girardi L., Salasnich B., Dal Cero C., Rubele S., Nanni A., 2012, MNRAS, 427, 127

Capuzzo-Dolcetta R., Spera M., 2013, Comput. Phys. Commun., 184, 2528

Capuzzo-Dolcetta R., Spera M., Punzo D., 2013, J. Comput. Phys., 236, 580

Chen Y., Bressan A., Girardi L., Marigo P., Kong X., Lanza A., 2015, MNRAS, 452, 1068

Dalessandro E. et al., 2016, ApJ, 833, 111

Davies R. et al., 2016, in Evans C. J., Simard L., Takami H., eds, Proc. SPIE Conf. Ser. Vol. 9908, Ground-based and Airborne Instrumentation for Astronomy VI. SPIE, Bellingham, p. 99081Z

De Marchi G. et al., 2016, MNRAS, 455, 4373

Devecchi B., Volonteri M., 2009, ApJ, 694, 302

Di Carlo U. N., Giacobbo N., Mapelli M., Pasquato M., Spera M., Wang L., Haardt F., 2019, MNRAS, 487, 2947

Diolaiti E. et al., 2016, in Marchetti E., Close L. M., Véran J.-P., eds, Proc. SPIE Conf. Ser. Vol. 9909, Adaptive Optics Systems V, SPIE, Bellingham, p. 990902

Fiorentino G., Tolstoy E., Diolaiti E., Valenti E., Cignoni M., Mackey A. D., 2011, A&A, 535, A63

Fiorentino G. et al., 2016, in Marchetti E., Close L. M., Véran J.-P., eds, Proc. SPIE Conf. Ser. Vol. 9909, Adaptive Optics Systems V. SPIE, Bellingham, p. 990906

Fiorentino G. et al., 2017, preprint (arXiv:1712.04222)

Giersz M., Leigh N., Hypki A., Lützgendorf N., Askar A., 2015, MNRAS, 454, 3150

Inno L. et al., 2016, ApJ, 832, 176

Khorrami Z., Vakili F., Chesneau O., 2016, preprint (arXiv:1605.07533)

Khorrami Z. et al., 2017a, Messenger, 168, 32

Khorrami Z. et al., 2017b, A&A, 602, 56

King I. R., 1966, AJ, 71, 64

Kroupa P., 2001, MNRAS, 322, 231

Mapelli M., 2016, MNRAS, 459, 3432

Marigo P. et al., 2017, ApJ, 835, 77

Massari D. et al., 2016a, A&A, 586, A51

Massari D. et al., 2016b, A&A, 595, L2

Miller M. C., Hamilton D. P., 2002, MNRAS, 330, 232

Monelli M. et al., 2015, ApJ, 812, 25

Monty S. et al., 2018, ApJ, 865, 160

Nitadori K., Makino J., 2008, New Astron., 13, 498

Pasquato M., Trenti M., De Marchi G., Gill M., Hamilton D. P., Miller M. C., Stiavelli M., van der Marel R. P., 2009, ApJ, 699, 1511

Portegies Zwart S. F., McMillan S. L. W., 2002, ApJ, 576, 899

Portegies Zwart S. F., Baumgardt H., Hut P., Makino J., McMillan S. L. W., 2004, Nature, 428, 724

Portegies Zwart S. F., McMillan S. L. W., Gieles M., 2010, ARA&A, 48, 431

Sabbi E. et al., 2016, ApJS, 222, 11

Saracino S. et al., 2015, ApJ, 806, 152

Schreiber L., Greggio L., Falomo R., Fantinel D., Uslenghi M., 2014, MNRAS, 437, 2966

Stetson P. B., 1987, PASP, 99, 191

Stetson P. B., 1994, PASP, 106, 250

Tang J., Bressan A., Rosenfield P., Slemer A., Marigo P., Girardi L., Bianchi L., 2014, MNRAS, 445, 4287

Turri P., McConnachie A. W., Stetson P. B., Fiorentino G., Andersen D. R., Véran J.-P., Bono G., 2015, ApJ, 811, L15

Volonteri M., 2010, A&AR, 18, 279

Volonteri M., Haardt F., Madau P., 2003, ApJ, 582, 559

Volonteri M., Lodato G., Natarajan P., 2008, MNRAS, 383, 1079

Zocchi A., Gieles M., Hénault-Brunet V., 2019, MNRAS, 482, 4713

This paper has been typeset from a TEX/LATEX file prepared by the author.